Planar 16-band metasurface-enhanced spectral filter for integrated image sensing

CHUFAN ZHOU,[1,*] OLIVIER J. F. MARTIN,[2] ⓘ
AND EDOARDO CHARBON[1] ⓘ

[1]*Advanced Quantum Architecture Laboratory (AQUA), Ecole Polytechnique Federale de Lausanne (EPFL), 2002 Neuchatel, Switzerland*
[2]*Nanophotonics and Metrology Laboratory, Swiss Federal Institute of Technology Lausanne (EPFL), EPFL-STI-NAM, Station 11, CH- 1015 Lausanne, Switzerland*
*chufan.zhou@epfl.ch

Abstract: We study theoretically and demonstrate experimentally a 16-band narrow band wavelength selective filter in the near-infrared range. The combination of a pair of distributed Bragg reflectors with a sub-wavelength grating metasurface embedded in the intra-cavity provides a narrow response which can be tuned by adjusting the geometry of the sub-wavelength grating metasurface. The key advantage of this approach is its ease of fabrication, where the spectral response is tuned by merely changing the grating period, resulting in a perfectly planar geometry that can be easily integrated with a broad variety of photodetectors, thus enabling attractive applications such as bio-imaging, time-of-flight sensors and LiDAR. The experimental results are supported by numerical simulations and effective medium theory that unveil the mechanisms that lead to the optical response of the device. It is also shown how the polarization dependence of the structure can be used to determine very accurately the polarization of incoming light.

1. Introduction

Multispectral imaging (MSI) and hyperspectral imaging (HSI) are imaging modalities requiring a large number of narrow filters coupled with image sensors; they are designed for applications, such as bio-imaging [1–3], food science [4–6], microscopy [7,8], and remote sensing [9]. While filters can be designed with a multitude of technologies, those based on Fabry-Perot (FP) cavities have gained attention due to their suitability for practical applications. FP cavities contain top and bottom symmetric distributed Bragg reflectors (DBRs) embedding different cavity thicknesses to achieve wavelength selectivity and tunability [10–12]. While a single wavelength FP filter can be realized with the mere planar deposition of different dielectric layers, the fabrication of a multispectral FP filter with different cavity thicknesses requires multiple photolithography and deposition steps, which makes their fabrication difficult. Recently, the utilization of metasurfaces within the cavity gained attention because it can be fabricated by a single e-beam lithography step, while still enabling a multispectral response [13]. Metasurface-based planar optics has found numerous applications, including wavelength selective filters [14–18], polarizers [19,20], photodetectors [21,22], metalenses [23–25] and metaholograms [20,26], Horie *et al.* [15] and Lee *et al.* [14] reported DBR-metasurface-DBR color filters working in the NIR range with a nano-post-based metasurface sandwiched in-between top and bottom DBRs. Yoon *et al.* introduced RGB filters with grating structures [16], while Hwang *et al.* [19] have reported double layer gold gratings for polarization-sensitive microgrid polarizers and have further discussed the incidence angle dependency of their device. However, only a few researchers discuss polarization dependency and wavelength selectivity simultaneously for metasurfaces sandwiched between DBRs.

In this work, we present planar DBR-metasurface-DBR structures and study their performance as wavelength-selective filters working in the NIR range (750-1000 nm). A high refractive

index contrast between Si and SiO$_2$ as DBR layers provides high wavelength selectivity. As metasurface, we embed sub-wavelength Si grating structures between the DBRs. Indeed, based on the effective medium theory (EMT), grating structures with different duty cycles tune the resonance wavelength by changing the equivalent refractive index of the cavity layer [27]. Since the different wavelength bands can be fabricated with one single step e-beam lithography, the designed structures are perfectly planar, although they work at different wavelengths, and enable on-chip integration. Grating structures also introduce a polarization dependency, which can influence spectral tunability, as will be discussed later. Different from previous studies, we confirm effective medium theory with measurement results. We also compare the designed structure to Fabry-Perot resonance by comparing transmittance spectral with different interval cavity thickness.

2.   Design and fabrication

2.1.   Fabry-Perot resonance and effective medium theory

In order to achieve narrow bandwith filters in the NIR band, we design top and bottom DBRs using Si and SiO$_2$ as high and low refractive index materials, as shown in Fig. 1. The thickness of Si and SiO$_2$ is designed at 55 nm and 100 nm, respectively. A metasurface structure is embedded within the cavity to achieve wavelength tunability, without altering either DBR structure and, most importantly, keeping the cavity thickness constant for all the different bands. The metasurface consists of a 1D subwavelength grating, whose period is tuned to control the spectral response of the system. Indeed, changing the period changes the effective medium value of the metasurface, which, in turn, alters the localized mode [18,27–32]. The metasurface is characterized by two parameters: the period P and the duty cycle D, *i.e.* the width of the Si grating elements divided by the period. At wavelengths shorter than the period, the transmission grating acts as a diffraction grating, which would be detrimental for the application considered here, since the optical energy would be spread among different diffraction orders. At longer wavelengths, the grating behaves like a homogeneous layer with an effective refractive index, which is controlled by D [18,32]. The light polarization is also important for such a system; Note that the definition of TE- and TM- polarization may differ from literatures; here, we define TE-polarization or 0° polarization as the electric field perpendicular to the grating structure, while the magnetic field is parallel to it. TM-polarization or 90° polarization is defined as the converse. The metasurface effective refractive indices n_{TE} and n_{TM} for each polarization can be summarized as [29]:

$$n_{TM}^2 = n_1^2(1 - D) + n_2^2 D, \tag{1}$$

$$n_{TE}^2 = \frac{n_1^2 n_2^2}{n_1^2 D + n_2^2 (1 - D)}, \tag{2}$$

where n_1 and n_2 represent the refractive index of the low (SiO$_2$) and high (Si) index materials, Thus, we are able to achieve wavelength tunability with different grating widths instead of changing the thickness of the cavity. Comparing Eq. (1) and (2), the equivalent refractive index under TM-polarization is different from that under TE-polarization, which indicates that the grating structure shows a polarization dependency.

2.2.   Fabrication process

We fabricate a 16-band DBR-metasurface-DBR wavelength selective filter using a fixed period $P = 400$ nm, and increasing the width of the Si grating elements from 200 nm to 350 nm (corresponding to varying D between 0.5 and 0.875) in 10 nm steps. The height of Si grating is designed at 55 nm. The top and bottom DBRs include each 3.5 Si/SiO$_2$ pairs with 55 nm thick Si and 100 nm thick SiO$_2$, as shown in Fig. 1(b). The fabrication process is briefly described here. The bottom Si/SiO$_2$ pairs DBR and the 55 nm Si layer that will be used as grating are
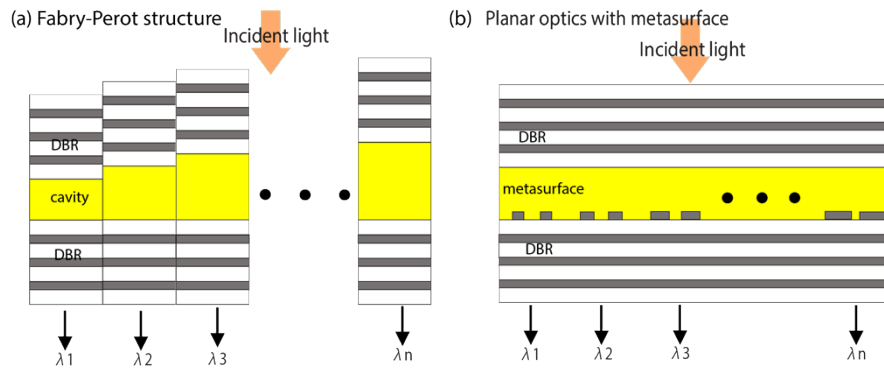
Fig. 1. (a) Schematic of FP structures for wavelength selective filters. Different cavity thicknesses are used to tune the center wavelength. (b) Schematic of the planar DBR-metasurface-DBR structure investigate in this work. Different grating width are used to tune the center wavelength.

deposited on a Borofloat wafer by PECVD (Oxford Plasmalab System 100) at 300∘C without breaking the vacuum. The Si grating structures with the 16 different duty cycles are fabricated by a single e-beam lithography process (Raith EBPG5000+): a 100 nm thick ZEP 520A (ZEON) e-beam resist is spin-coated on the surface as hard mask. A 8 nm thick Cr layer is evaporated (Alliance-Concept EVA 760) on top of the photoresist to avoid charging during the exposure and then removed with TechniEtch Cr01 ($(NH_4)_2Ce(NO_3)_6 + HClO_4$) at room temperature before resist development (Amyl-Acetate and 90:10 MiBK:IPA rinse solution). An etching process by ion beam etcher (Veeco Nexus IBE350) follows to carve the 16 grating structures. A planarization step is required once the Si gratings have been fabricated. This is performed with SiO_2 using PECVD (Oxford Plasmalab System 100). We planarize the cavity to two different SiO_2 thicknesses (360 nm and 600 nm) in order to investigate the influence of that cavity thickness on wavelength tunability. Lastly, we deposit the top DBR by PECVD (Oxford Plasmalab System 100). Note that this process can easily be applied to a large area, which is important to cover large image sensors with resolutions of several megapixels [33].

3. Results and discussion

3.1. Wavelength selectivity and tunability

Figure 2 and Fig. 3 below provides the transmittance measured with a spectrometer (FilMetrics F20-UV) at normal incident light under different incident light polarizations with a polarizer (LPNIRE2 × 2, Thorlab). The spot size of the spectroscopy light source is 1.5 mm, which is larger than the pattern we fabricated. Note that narrow spectral lines are obtained, with a full width at half-maximum of 6-16 nm for TE-polarization and 7-15 nm for TM polarization with 360 nm cavity, 6-9 nm for TE-polarization and 6-7 nm for TM polarization with 600 nm cavity. These spectral bands are distributed continuously and uniformly over a range that can be tuned by adjusting the thickness of the metasurface cavity embedded between the two DBRs, as will be discussed below.

Figure 2(a) shows the SEM image of one grating structure, taken before the planarization of the cavity layer. A 5 nm Cr layer is sputtered on top of the structure to avoid charging during SEM imaging. In Fig. 2(b) and 2(c), we compare the measured transmittance with that computed by the finite-difference time domain (FDTD) method (Ansys Lumerical 2022 R1.3 Finite) for both TE- and TM-polarizations as a function of the width of the Si grating element between

200 nm and 350 nm. We set the mesh size to 10 nm in the simulations. The vertical axis in these heat maps corresponds to the wavelength and the color bar shows the transmittance magnitude.
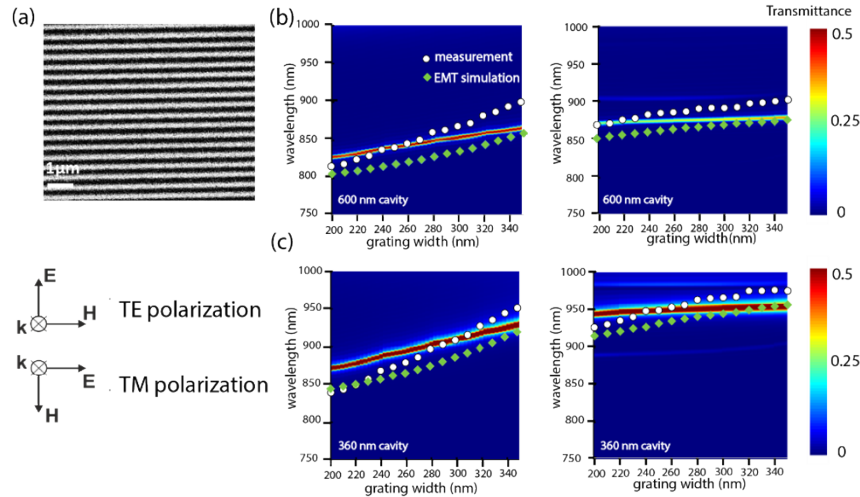

Fig. 2. (a) SEM image of one representative fabricated grating structure and definition of the TE- and TM-polarizations. Simulated and measured transmittances for structures with a (b) 600 nm and (c) 360 nm cavity under TE- (left) and TM-polarizations (right). White dots on the heat map represent each measured center wavelength among the 16 bands. Green dots on the heat map represent each simulated center wavelength of EMT simulation.

Using these simulations, we first compare the wavelength selectivity and tunability obtained from numerical simulations for TE- and TM-polarizations. The resonance wavelength under TE-polarization is tuned from 870 to 929 nm (tuning range 59 nm) with a 360 nm cavity and from 826 to 866 nm (tuning range 40 nm) with a 600 nm cavity. The resonance wavelength under TM-polarization is tuned from 943 to 954 nm (tuning range 11 nm) with a 360 nm cavity, and from 870 to 880 nm (tuning range 10 nm) with a 600 nm cavity. We conclude that transmittance under TE-polarization shows a higher tuning range than under TM-polarization, where it is less than 10 nm. This is confirmed by the measurements, shown as white dots in Figs. 2(b), (c), yielding the following values for the corresponding tuning ranges: 113 nm, respectively 85 nm, for TE-polarization for a 360 nm, respectively 600 nm cavity. For TM-polarization, the experimental tuning ranges are 49 nm for the 360 nm cavity and 34 nm for the 600 nm cavity. The agreement between simulations and experiments is fair, taking into account the complexity of the latter, which includes many sensitive steps that can influence the overall device transmissivity.

We also simulated the transmittance spectrum with EMT by changing the 55 nm high metasurface layer to an artificial layer with the calculated refractive index listed in the Supplement 1, Table S1. The refractive index of Si and SiO_2 is set to 3.8 and 1.48, respectively. We plot the simulated resonance wavelength on the heat map for comparison. As we change the duty cycle of the metasurface from 0.5 to 0.875, the effective refractive index changed from 1.95 to 2.91 under TE-polarization, 2.88 to 3.59 under TM-polarization. Simulation results agree with experimental results in that the TE-polarization has a relatively larger wavelength tunability. Resonance wavelengths under TM-polarization appear at longer wavelengths due to larger effective refractive index. Simulation result with EMT highly agree with simulations in the heat map indicates that EMT model is well suited for metasurface design.

Both measurements and simulations indicated that the devices with a thinner cavity has larger tunability. Furthermore, the transmittance is larger and the FWHM is wider for the 360 nm

cavity, compared to the 600 nm cavity. The transmittance resonance difference under TM- and TE-polarizations for each band enables the utilization of this device for polarization detection, as will be discussed in the next section.

Figure 3 shows the full spectra response at 500-1000 nm from (a) measurement, (b) simulated 16 band with FDTD and (c) simulated 16 band with EMT. Discrepancies between the experimental results and the numerical simulations may resulted by fabrication error and Si parameter uncertainties. Almost no transmittance been visualized at lower wavelength (500–700 nm) in measurement result, however, we can see transmittance at lower wavelength band in both FDTD and EMT simulation. This indicates that the refractive index of material varied from simulation and measurement. Result from EMT model is relatively close to FDTD simulation result. Fabrication error also cause discrepancies between experimental results and numerical simulation results. Fabrication error in the thickness of DBR layer cause the resonance wavelength shift to shorter or longer wavelength, all the wavelength will shift together. Fabrication error in grating size will influence the wavelength tunability. Detailed simulation is discussed in Supplymental Document Fig.S1. The current transmittance of designed structure is low due to the absorptance of selected material, to better improve the transmittance we can use all-dielectric material or decrease the DBR pair. We can also decrease the thickness of interval cavity for higher transmittance. Regarding to simulation and measurement results, transmittance spectra with 360 nm cavity is higher than that of 600 nm cavity.
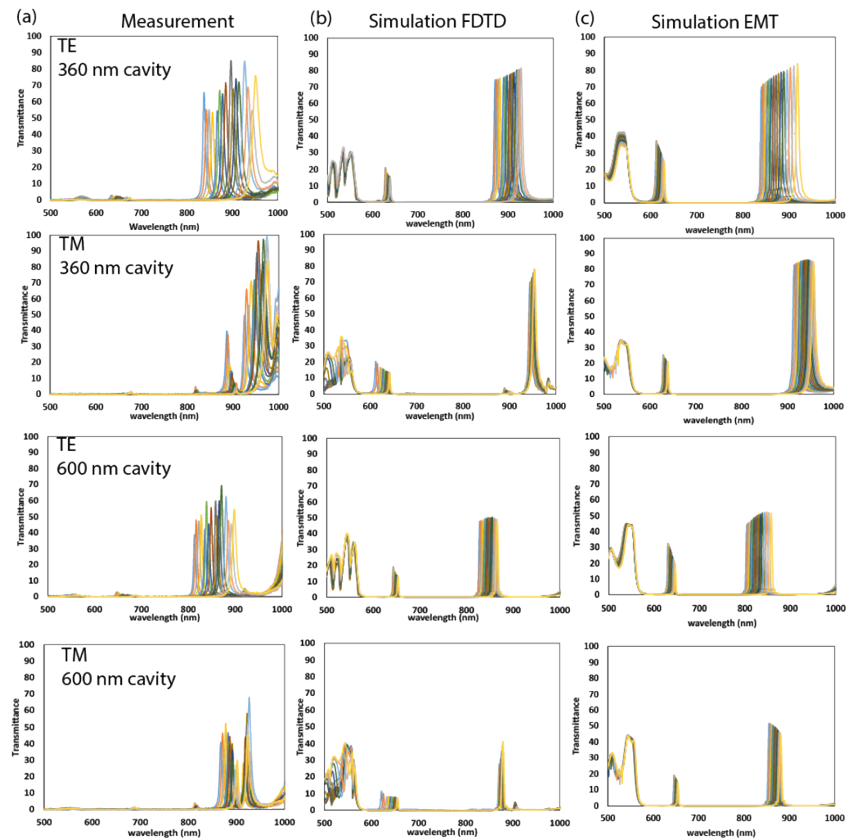

Fig. 3. Full spectra response at 500 -1000 nm from (a) measurement (b) simulated results with FDTD method (c) simulated results with EMT method.

A single device with 16 different spectral responses distributed continuously and uniformly is fabricated with one single e-beam step. The different spectra are obtained by tuning the properties of the metasurface inside the cavity between two DBRs. Two different cavity thicknesses are investigated: 360 nm and 600 nm. The former has the highest transmittance, while the latter has narrower full width at half maximum (FWHM) resonances. For the 360 nm cavity the FWHM ranges between 6 and 16 nm, while for the 600 nm cavity it is between 6 and 9 nm under TE-polarization.

3.2. Polarization dependency

In order to further analyze the polarization dependency, we select a 600 nm cavity, a 200 nm grating size and we measure the transmittance spectrum $T_0(\lambda)$ under 0° polarization (TE) or under 90° polarization (TM) $T_{90}(\lambda)$, see Fig. 4(b) top. Then, we measure the transmittance $T_\theta(\lambda)$ for three arbitrarily chosen polarization angles 32°, 52° or 67°, Fig. 4(b) bottom. The transmittance spectrum under different angles can be reconstructed by the combination of the transmittance spectra for 0° and 90° polarizations: $T_\theta(\lambda) = T_0(\lambda)cos^2\theta + T_{90}(\lambda)sin^2\theta$ [27]. Since $cos^2\theta + sin^2\theta = 1$, we can estimate the polarization angle of the incident light by comparing the measured intensity with either that of the 0° or 90° references.
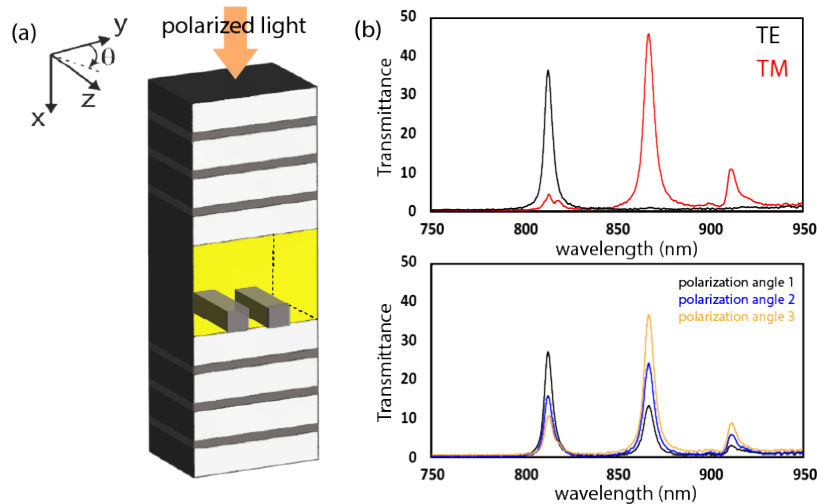

Fig. 4. (a) Schematic of DBR-metasurface-DBR with incident polarized light, including the definition of the polarization angle θ. (b) Top: measured transmittance for a device with a 600 nm cavity and a 200 nm grating width, under TE- and TM-polarizations. Bottom: transmittance of same structure for three different arbitrarily chosen polarization angles.

Table 1 shows the values for $cos^2\theta$ and $sin^2\theta$ calculated by dividing the measured intensity by the intensities for 0° and 90°, for the three arbitrarily chosen polarization angles. An average value can be found form these two values and we can compute the error $\Delta\theta$ between that average value and the exact angle. From this table, we note that the error between the measured ($\theta_{arccos\theta}$ and $\theta_{arcsin\theta}$) and real angles (θ_{select}) is extremely small, below 7°! As expected, the designed structure functions as a polarization detector and we can estimate the unknown polarization angle by estimating the intensity at 0° and 90°. Based on this structure we can measure simultaneously the resonance wavelength and the polarization angle.

We choose 4 wavelength 360 nm cavity and 600 nm cavity with 200 nm grating size under TE- and TM- polarization to estimate the polarization extinction ratio (PER) shown in Fig. 5. For

Table 1. $cos^2\theta$ and $sin^2\theta$ calculated from measurement data

θ_{select}	$cos^2\theta$	$\theta_{arccos\theta}$	$\Delta\theta$	$sin^2\theta$	$\theta_{arcsin\theta}$	$\Delta\theta$
32°	0.657	35.8°	3.8°	0.308	33.7°	1.7°
52°	0.382	51.8°	0.2°	0.560	48.4°	3.6°
67°	0.245	60.3°	6.7°	0.798	63.2°	3.8°

each structure we calculate the PER of different polarization at center wavelength with equations:

$$PER_{TE} = 10\ log_{10}\frac{P_{TE\ center}}{P_{TM\ center}} \tag{3}$$

$$PER_{TM} = 10\ log_{10}\frac{P_{TM\ center}}{P_{TE\ center}} \tag{4}$$

$P_{TE\ center}$ and $P_{TM\ center}$ on numerator represent the transmittance of center wavelength. $P_{TM\ center}$ and $P_{TE\ center}$ on denominator represent the transmittance of selected center wavelength at the other polarization incident. Result shows that PER_{TE} at 360 nm is 16.5 dB, at 600 nm is 10.5 dB. PER_{TM} at 360 nm is 16.6 dB, at 600 nm is 17.1 dB.
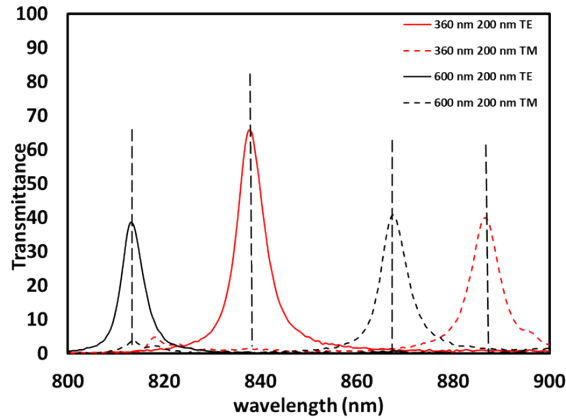

Fig. 5. Selected wavelength for with 360 nm cavity and 600 nm cavity with 200 nm grating size under TE-polarization and TM polarization.

Lastly, we discuss the electric field propagation along the DBR-metasurface-DBR structure in the x-direction (monitor A) and inside the metasurface in the y-z plane (monitor B) for different polarization conditions. The intensity of the electric field is evaluated using numerical method with the same mesh setting as descried previously. We simulate in Fig. 6 the DBR-metasurface-DBR structures for a 200 nm grating and a 600 nm cavity, panels (a) and (b), or a 360 nm cavity, panels (c) and (d). For the 600 nm cavity, the resonance wavelength appears at 826 nm under TE-polarization and at 870 nm under TM-polarization. For TE-polarization, the normalized electric field along the x-axis exhibits similar features as a FP resonance, Fig. 6(a) monitor A, with 3 modes inside the cavity. The electric field inside the metasurface is confined in the low refractive index material (SiO$_2$) region since the electric flux is constant along the y-direction, Fig. 6(a) monitor B. Under TM-polarization, the grating structure breaks the electric field symmetry along the x-direction and exhibits Talbot patterns [34]. As a result, the periodic grating structure reforms a copy of itself downstream into the bottom DBR, Fig. 6(b) monitor A. The structure with a 360 nm cavity layer shows the same properties, with 2 modes in the FP cavity under TE-polarization, due to the reduced thickness of the cavity layer.
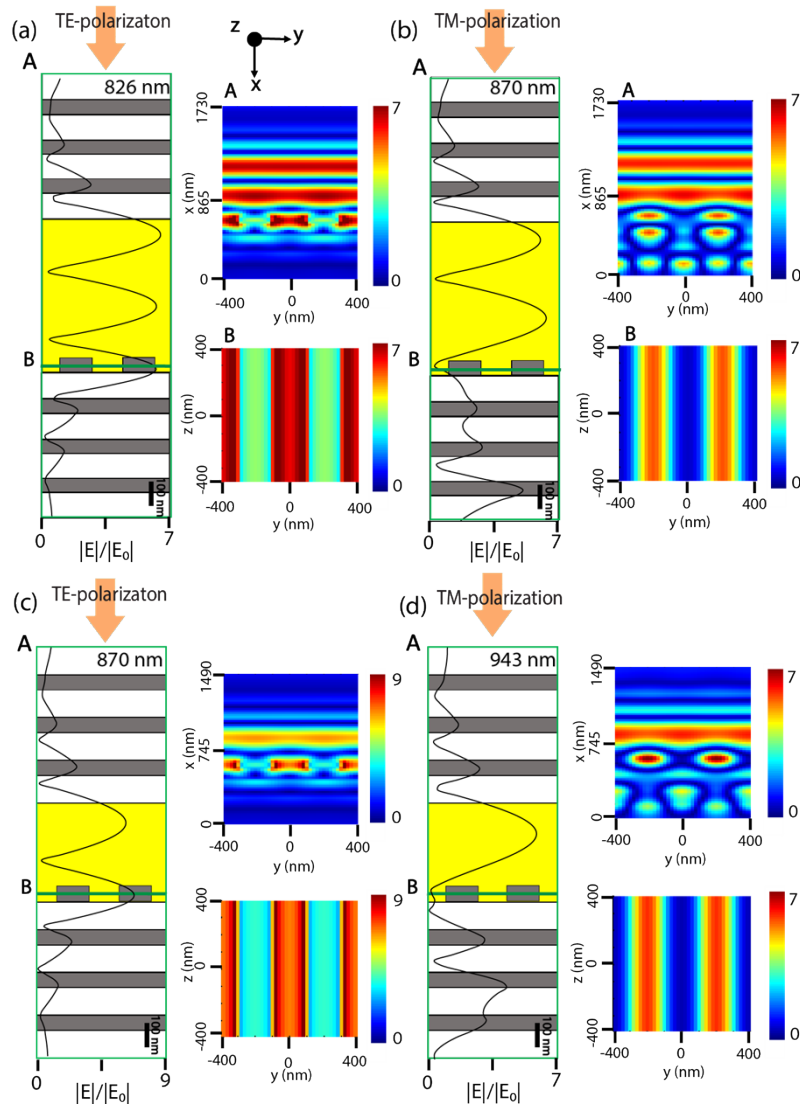
Fig. 6. Schematic of the DBR-metasurface-DBR structure with a 200 nm grating width and (a, b) a 600 nm or (c, d) a 360 nm cavity. Normalized electric field profiles $|E|/|E_0|$ at the resonance wavelength of (a) 826 nm under TE-polarization, (b) 870 nm under TM-polarization, (c) 870 nm under TE-polarization, and (d) 943 nm under TM-polarization. The monitor A illustrate the electric field density along the DBR-metasurface-DBR structure in the x-direction, while the monitor B illustrates the electric field density propagating within the metasurface (y-z plane)

4. Conclusions

We have designed and experimentally demonstrated a planar polarization-dependent 16-band wavelength selective filter with a DBR-metasurface-DBR structure. The DBR included 3.5 pairs of Si/SiO$_2$ multilayers, while the metasurface was built from a subwavelength Si grating with different width to control the spectral response. Wavelength selectivity and tunability have been achieved through the combination of the DBR and the metasurface. We have discussed

the key parameters that control the response of that system and how its operation range can be tuned by modifying the thickness of the cavity that holds the metassurface. Structures with thinner cavity result in higher tunability. We also discussed the polarization dependency by comparing the spectral response and the electric field density inside the structure under TE- and TM-polarizations. Using the response of the device under those two orthogonal polarizations, we were able to retrieve the polarization angle for arbitrary illumination, thus making this device a useful polarization analysis tool that can simultaneously measure the resonance wavelength and the polarization angle of incident light. This 16-band planar filter is fabricated with one single e-beam lithography step and produces a perfectly planar structure, which can be easily integrated with a broad variety of photodetectors, paving the way for lab-on-chip applications, polarization dependent imaging and other novel imaging applications.

Disclosures. The authors declare no competing interests.

Data availability. The experimental data that support the findings presented here are available from the corresponding authors upon reasonable request.

Supplemental document. See Supplement 1 for supporting content.

References

1. Z. Yang, T. Albrow-Owen, W. Cai, *et al.*, "Miniaturization of optical spectrometers," Science **371**(6528), eabe0722 (2021).
2. G. Lu and B. Fei, "Medical hyperspectral imaging: a review," J. Biomed. Opt. **19**(1), 010901 (2014).
3. T. Vo-Dihn, D. L. Stokes, M. B. Wabuyele, *et al.*, "A hyperspectral imaging system for in vivo optical diagnostics," IEEE Eng. Med. Biol. Mag. **23**(5), 40–49 (2004).
4. B. Lu, P. Dao, J. Liu, *et al.*, "Recent advances of hyperspectral imaging technology and applications in agriculture," Remote Sens. **12**(16), 2659 (2020).
5. J. Ma, D.-W. Sun, H. Pu, *et al.*, "Advanced techniques for hyperspectral imaging in the food industry: principles and recent applications," Annu. Rev. Food Sci. Technol. **10**(1), 197–220 (2019).
6. Y.-Z. Feng and D.-W. Sun, "Application of hyperspectral imaging in food safety inspection and control: a review," Crit. Rev. Food Sci. Nutr. **52**(11), 1039–1058 (2012).
7. S. J. Leavesley, N. Annamdevula, J. Boni, *et al.*, "Hyperspectral imaging microscopy for identification and quantitative analysis of fluorescently-labeled cells in highly autofluorescent tissue," J. Biophotonics **5**(1), 67–84 (2012).
8. W. Jahr, B. Schmid, C. Schmied, *et al.*, "Hyperspectral light sheet microscopy," Nat. Commun. **6**(1), 7990 (2015).
9. C. González, S. Sánchez, A. Paz, *et al.*, "Use of FPGA or GPU-based architectures for remotely sensed hyperspectral image processing," Integration **46**(2), 89–103 (2013).
10. G. Hernandez, *Fabry-Perot Interferometers*, 1. paperback ed. Cambridge Studies in Modern Optics No. 3 (Cambridge Univ. Press, 2011).
11. J. M. Vaughan, *The Fabry-Perot Interferometer: History, Theory, Practice, and Applications*, The Adam Hilger Series on Optics and Optoelectronics (A. Hilger, 1989).
12. H. A. Macleod, *Thin-Film Optical Filters*, Fifth edition, Series in Optics and Optoelectronics (CRC Press, Taylor & Francis Group, 2018).
13. N. Yu and F. Capasso, "Flat optics with designer metasurfaces," Nat. Mater. **13**(2), 139–150 (2014).
14. J. Lee, Y. Park, H. Kim, *et al.*, "Compact meta-spectral image sensor for mobile applications," Nanophotonics **11**(11), 2563–2569 (2022).
15. Y. Horie, A. Arbabi, E. Arbabi, *et al.*, "Wide bandwidth and high resolution planar filter array based on DBR-metasurface-DBR structures," Opt. Express **24**(11), 11677 (2016).
16. Y.-T. Yoon, C.-H. Park, and S.-S. Lee, "Highly efficient color filter incorporating a thin metal–dielectric resonant structure," Appl. Phys. Express **5**(2), 022501 (2012).
17. T. Xu, Y.-K. Wu, X. Luo, *et al.*, "Plasmonic nanoresonators for high-resolution colour filtering and spectral imaging," Nat. Commun. **1**(1), 59 (2010).
18. T. K. Gaylord, W. E. Baird, and M. G. Moharam, "Zero-reflectivity high spatial-frequency rectangular-groove dielectric surface-relief gratings," Appl. Opt. **25**(24), 4562 (1986).
19. J. Hwang, B. Oh, Y. Kim, *et al.*, "Fabry-Perot cavity resonance enabling highly polarization-sensitive double-layer gold grating," Sci. Rep. **8**(1), 14787 (2018).
20. J. Hwang, Z. Ku, J. Jeon, *et al.*, "Polarization-Sensitive and Wide Incidence Angle-Insensitive Fabry–Perot Optical Cavity Bounded by Two Metal Grating Layers," Sensors **20**(18), 5382 (2020).
21. C.-Y. Li, C. Chen, Y. Liu, *et al.*, "Multiple-polarization-sensitive photodetector based on a perovskite metasurface," Opt. Lett. **47**(3), 565 (2022).
22. X. Xu, H. Kwon, B. Gawlik, *et al.*, "Enhanced photoresponse in metasurface-integrated organic photodetectors," Nano. Lett. **18**(6), 3362–3367 (2018).
23. F. Capasso, "The future and promise of flat optics: a personal perspective," Nanophotonics **7**(6), 953–957 (2018).

24. M. Khorasaninejad and F. Capasso, "Metalenses: Versatile multifunctional photonic components," Science **358**(6367), eaam8100 (2017).
25. W. T. Chen, A. Y. Zhu, V. Sanjeev, *et al.*, "A broadband achromatic metalens for focusing and imaging in the visible," Nat. Nanotech. **13**(3), 220–226 (2018).
26. M. Khorasaninejad, A. Ambrosio, P. Kanhaiya, *et al.*, "Broadband and chiral binary dielectric meta-holograms," Sci. Adv. **2**(5), e1501258 (2016).
27. C. W. Haggans, R. K. Kostuk, and L. Li, "Effective-medium theory of zeroth-order lamellar gratings in conical mountings," J. Opt. Soc. Am. A **10**(10), 2217 (1993).
28. P. Lalanne and D. Lemercier-lalanne, "On the effective medium theory of subwavelength periodic structures," J. Mod. Opt. **43**(10), 2063–2085 (1996).
29. H. Kikuta, Y. Ohira, H. Kubo, *et al.*, "Effective medium theory of two-dimensional subwavelength gratings in the non-quasi-static limit," J. Opt. Soc. Am. A **15**(6), 1577 (1998).
30. C. L. Holloway, E. F. Kuester, J. A. Gordon, *et al.*, "An overview of the theory and applications of metasurfaces: the two-dimensional equivalents of metamaterials," IEEE Antennas Propag. Mag. **54**(2), 10–35 (2012).
31. P. Lalanne and J.-P. Hugonin, "High-order effective-medium theory of subwavelength gratings in classical mounting: application to volume holograms," J. Opt. Soc. Am. A **15**(7), 1843 (1998).
32. S. Collin, "Nanostructure arrays in free-space: optical properties and applications," Rep. Prog. Phys. **77**(12), 126402 (2014).
33. K. Morimoto, A. Ardelean, M.-L. Wu, *et al.*, "Megapixel time-gated SPAD image sensor for 2D and 3D imaging applications," Optica **7**(4), 346 (2020).
34. J. Wen, Y. Zhang, and M. Xiao, "The Talbot effect: recent advances in classical optics, nonlinear optics, and quantum optics," Adv. Opt. Photonics **5**(1), 83 (2013).